Supporting Information

Jürgen Reingruber, Johan Pahlberg, Michael Woodruff,
Alapakkam P. Sampath, Gordon L. Fain, David Holcman

We present here the details of our modeling, data analysis and simulations of the photoresponse and dark noise. We start by presenting our model based on spatially resolved reaction-diffusion equations. The model accounts for the fundamental constraints imposed by the rod geometry and the biochemistry of the transduction cascade. We further present stochastic simulations of the molecular network leading to PDE activations, a required step to derive the dark noise and the variability of the photoresponse. Finally, we derive analytical expressions from the power spectrum of the dark current to extract key parameters that we use in simulations.

1 Modeling of the single-photon response (SPR) and dark noise

Coarse graining the outer segment (OS) geometry

The geometry of the rod OS is divided by internal parallel disks into compartments connected to each other through narrow gaps between the disk rim and the OS membrane and through incisures (Fig. S1). This compartmentalization reduces the diffusion of cGMP and calcium between compartments, whereas diffusion within a compartment is not hindered and produces rapid equilibration. We therefore adopt the approximation of a transversally well stirred OS where the three-dimensional geometry can be reduced to an effective one-dimension model [1]. The number of disk incisures varies considerably among species. Whereas toad and amphibian rods can have up to 30 incisures, a mouse rod has only a single incisure [2, 3, 4, 5]. Incisures have two main effects: first, they facilitate longitudinal diffusion between the disks [6, 7]; and second, they hinder the diffusion of proteins on the disk membrane and thereby affect PDE activation [8, 9]. The major effect of incisures is the facilitation of longitudinal diffusion [7, 6], and in our model we incorporate this feature of outer segment structure by using an effective longitudinal diffusion constant for cGMP and calcium. In mouse, because there is only a single incisure, restriction of membrane diffusion due to incisures is not important [10]. However, even in amphibian rods with many incisures, diffusional restriction due to incisures does not significantly affect the photoresponse [7]. This result is probably a consequence of the fast transversal cGMP diffusion, in which case the the position on the disk were PDE is activated does not much affect the rate of cGMP hydrolysis. In addition, because the dark noise is generated by fast and uniformly distributed spontaneous PDE activations and deactivations, it is also little affected by diffusional restrictions due to incisures.

The concentration of cGMP is modeled by an effective longitudinal reaction-diffusion equation with calcium-dependent synthesis catalyzed by guanylyl cyclase (GC) and with hydrolysis catalyzed by light-activated and spontaneously activated phosphodiesterase (PDE), with GC and PDE both located on the surface of the disk membrane (see [11, 12]). Calcium dynamics also follows effective longitudinal diffusion with additional source terms arising from the currents through the cGMP-gated channels and the $Na^+Ca^{2+}K^+$-exchanger. Because an effect of calcium on spontaneous PDE
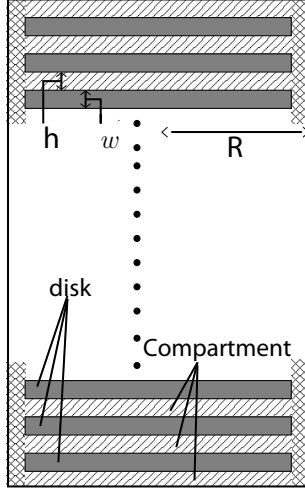
Fig. S1: **Compartmental model of a rod outer segment.** We show a section through a cylindrical rod outer segment, containing a stack of parallel and uniformly distributed disks. The domain delimited by two adjacent disks will be referred to as a compartment.

activation has not yet been conclusively demonstrated (though see [13]), we do not account for this possibility in our model.

Stochastic model for spontaneous PDE activation

PDE molecules activate and deactivate spontaneously with Poisson rates ν_{sp} and μ_{sp} according to the biochemical reaction

$$PDE \quad \underset{\mu_{sp}}{\overset{\nu_{sp}}{\rightleftharpoons}} \quad P^*_{sp}. \tag{1}$$

We use Eq. 1 together with the Gillespie algorithm [14] to simulate the time course of the stochastic number of spontaneously activated PDE in a compartment. The average number of spontaneously activated PDE in a compartment is [15]

$$\bar{P}^*_{sp,comp} = 2\rho_{pde}\pi R^2 \frac{\nu_{sp}}{\mu_{sp}}, \tag{2}$$

where ρ_{pde} is the PDE surface density and R is the compartment radius. For example, for toad rods, assuming $\nu_{sp} = 4 \times 10^{-4}s^{-1}$ and $\mu_{sp} = 1.8s^{-1}$ [15], $R = 3\mu m$ and $\rho_{pde} = 100\mu m^{-2}$ (see Table S3), we find $\bar{P}^*_{sp,comp} = 1.25$. Fig S2a shows a simulation of the stochastic number of spontaneously activated PDE in a toad compartment with $\bar{P}^*_{sp,comp} = 1.25$ and $\mu_{sp} = 1.8s^{-1}$, and Fig S2b corresponds to a mouse compartment with $\bar{P}^*_{sp,comp} = 0.9$ and $\mu_{sp} = 12.4s^{-1}$ (see Table S3).

Stochastic model for PDE activation following a photon absorption

To simulate the time course of the stochastic number of activated PDE after a photon absorption (denoted shortly by light-activated PDE), we use the model previously described in [16] (see also
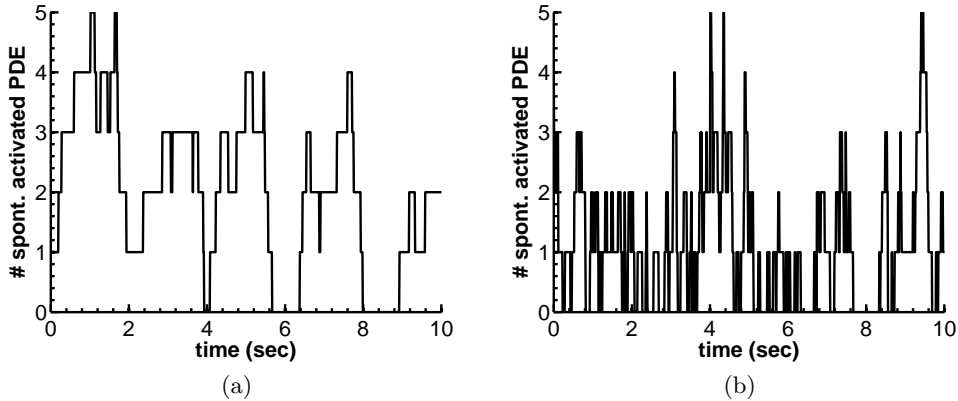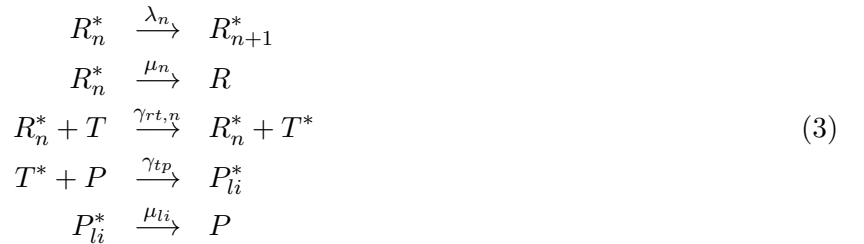
Fig. S2: **Spontaneous PDE activation.** (a) Simulation of the stochastic number of activated PDE in a toad compartment with $\bar{P}^*_{sp,comp} = 1.25$ and $\mu_{sp} = 1.8s^{-1}$. (b) Simulation of the stochastic number of activated PDE in a mouse compartment with $\bar{P}^*_{sp,comp} = 0.9$ and $\mu_{sp} = 12.4s^{-1}$.

[17, 18, 19, 20, 21]). A list of all of the parameters is given in Tables S1 and S2, their values are given in Tables S3 and S4.

Biochemical reactions leading to PDE activation following a photon absorption

The biochemical reactions leading to PDE activation that we considered in our model are the following: An activated rhodopsin R^* activates PDE via a G-protein coupled amplification cascade. R^* activity becomes gradually quenched via N_p phosphorylation steps catalyzed by rhodopsin kinase (RK), and finally rhodopsin is deactivated through arrestin binding. We neglect calcium feedback on the PDE activation process [22, 23, 24, 25]. Depending on the number of phosphorylations $n = 0, \ldots, N_p$, activated rhodopsin is in state R^*_n. The phosphorylation rates λ_n and the transducin activation rates $\gamma_{rt,n}$ depend on the phosphorylation state. Eventually R^*_n becomes deactivated through arrestin binding with a phosphorylation dependent rate μ_n. The kinetic reactions are

$$
\begin{aligned}
R^*_n &\xrightarrow{\lambda_n} R^*_{n+1} \\
R^*_n &\xrightarrow{\mu_n} R \\
R^*_n + T &\xrightarrow{\gamma_{rt,n}} R^*_n + T^* \\
T^* + P &\xrightarrow{\gamma_{tp}} P^*_{li} \\
P^*_{li} &\xrightarrow{\mu_{li}} P
\end{aligned}
\tag{3}
$$

We apply Eq. 3 together with the Gillespie algorithm [14] to simulate the time course of the number of light-activated PDE after a photon absorption.

Choice of parameter values

We now briefly explain how we chose the parameter values for the simulations (for a more detailed discussion see [16]): We used $N_p = 6$ and assumed that λ_n and $\gamma_{rt,n}$ decay exponentially with rate

3

$\omega = 0.1$ as a function of n and arrestin binds only when R^* is fully phosphorylated; so

$$
\begin{array}{rcll}
\lambda_n & = & \lambda_{max} e^{-\omega n}, & 0 \le n \le N_p - 1 \\
\gamma_{rt,n} & = & \gamma_{rt,max} e^{-\omega n}, & 0 \le n \le N_p \\
\mu_n & = & \delta_{nN_p} \lambda_{max} e^{-\omega N_p}.
\end{array}
\tag{4}
$$

The mean R^* lifetime computed in [16] is

$$
\tau_{rh} = \frac{1}{\lambda_{max}} \frac{1 - e^{\omega N_p}}{1 - e^{\omega}}.
\tag{5}
$$

For a measured R^* lifetime, we use Eq. 5 to calibrate λ_{max} such that the mean lifetime equals the measured lifetime. Finally, we use $\gamma_{rt,max}$ to adapt the mean maximal number of light-activated PDE $P^*_{li,max}$ during the time response.

For mouse rod, the measured R^* lifetime is $\tau_{rh} = 40ms$ [26, 27] and the lifetime of light-activated PDE is $\mu_{li}^{-1} = 200ms$ [28, 27, 29, 30]. For toad τ_{rh} is not precisely known, for example, a value of 2.5 seconds is estimated in [31], and in [23] a range between 0.8-3 seconds is found with a mean of around 1.7 seconds. For the lifetime of activated PDE (μ_{li}^{-1}) in toad we found in the literature the value 1 second given in [23], and in [31] a lifetime around 2.1 second is estimated. For the lifetime of light-activated PDE in a salamander rod we found 1.5 seconds [32] and 1.6 seconds [33]. In general, to obtain a photoresponse with a peak around 2 seconds and a duration around 5 seconds when the PDE lifetime is around 1-2 seconds, we must have an activated rhodopsin lifetime around 2-3 seconds. For the toad simulations, we therefore use $\tau_{rh} = 2.5sec$ and $\mu_{li}^{-1} = 1.6s^{-1}$. With these toad values we could additionally explore the impact of two very different sets of conditions for excitation of the transduction cascade: in mouse the R^* lifetime is smaller than the P^*_{li} lifetime, and in toad it is opposite. As shown in [16], this difference has significant implications for the value of the coefficient of variation (CV) of the peak number of P^*_{li}, because the CV can be much smaller in toad compared to mouse (see Fig. 2e in [16] for the CV in toad, and Eq. 58 for mouse). If R^* deactivation is rate limiting, the variability in PDE activation during the initial phase up to the peak can be very low, and in this case much of the variability is shifted to the recovery phase. However, when P^*_{li} deactivation is rate limiting the CV of the peak number of P^*_{li} is higher and limited by the number of deactivation steps [16].

The toad simulations in Fig. 1 in the main text with $\beta_d = 1s^{-1}$ show that $P^*_{li,max} \sim 150$ is needed to produce a single-photon response that reduces the current by around 5% [34, 23], which is achieved with $\gamma_{rt,max} \sim 200s^{-1}$. Such a value for the maximal transducin activation rate is still compatible with experimental data, suggesting that transducin activation proceeds with a mean rate $\sim 120s^{-1}$ [35]. In section 6 we show that the reduced value $\gamma_{rt,max} \sim 80s^{-1}$ would already be sufficient to produce a single-photon response that reduces the current by around 5% in case of $\beta_d = 0.5s^{-1}$. In mouse, a rate $\gamma_{rt,max} = 200s^{-1}$ would lead to $\bar{P}^*_{li,max} \approx 5$, which is not sufficient to match the single-photon response amplitude of our experimental recordings (Fig. 4A in the main text) with the simulations (Fig. 4B in the main text). We estimated that in mouse we need a rate $\gamma_{rt,max} = 350s^{-1}$ leading to $\bar{P}^*_{li,max} \approx 8.2$, a factor 1.75 higher compared to toad. Higher transducin activation rates in mouse compared to toad could result from the higher mouse body temperature [24, 35, 36, 37, 38].

cGMP hydrolysis by spontaneously and light-activated PDE

A key feature of this work is that we model cGMP hydrolysis by spontaneously and light-activated PDE with different rate constants denoted by k_{sp} and k_{li}.

cGMP hydrolysis by light-activated PDE

Light-activated PDE is an extremely efficient enzyme with a maximal turnover rate of the order of $k_{cat} \sim 2200 s^{-1}$ [35]). This suggests that cGMP hydrolysis by light-activated PDE is limited by the diffusional encounter rate k_{enc}. The average encounter rate between an activated PDE molecule on the disk surface and a single cGMP molecule diffusing in the cytoplasm is defined by the geometry of the compartment and is given by [39, 1]

$$k_{enc} = \frac{D_g}{R^2} \left(\pi \frac{h}{a} \frac{a_0(h/a)}{\sqrt{2}} + \frac{4 \ln(R/a) - 3}{8} \right)^{-1}, \tag{6}$$

where a is the reaction radius (in first approximation this is the sum of the radii of a PDE and a cGMP molecule) and h the compartment height (with $a = 3nm$ and $h = 15nm$ we have $a_0(h/a) \approx 0.7$ [39]). For a toad rod, we compute $k_{enc} \approx 2.9 s^{-1}$, and for a mouse with smaller OS radius we find $k_{enc} \approx 61 s^{-1}$. Our calculated rate $k_{enc} = 61 s^{-1}$ for mouse is close to the hydrolysis rate $43 s^{-1}$ estimated previously [29]. To obtain the total encounter rate between activated PDE and cGMP, we need to multiply k_{enc} with the number of cGMP molecules in a compartment. For a toad rod with a dark cGMP concentration around $3 \mu M$ [32, 40, 41] we find 250 cGMP molecules per compartment, and the overall encounter rate is $2.9 \times 250 s^{-1} = 740 s^{-1}$, much less than k_{cat}. This shows that in a toad compartment cGMP hydrolysis by light-activated PDE is indeed diffusion limited (this would not be true if the overall rate would be larger than k_{cat}). Because $k_{enc} \sim R^{-2}$ and $V_{comp} \sim R^2$, the overall cGMP hydrolysis rate is independent of the compartment radius, and our conclusion therefore also applies to other rods with the same dark cGMP concentration but a different OS radius. In particular, this finding shows that cGMP hydrolysis in the smaller-diameter mouse outer segment compartment is also diffusion limited. In summary, cGMP hydrolysis by light-activated PDE is diffusion limited and is given by the encounter rate, $k_{li} = k_{enc}$.

cGMP hydrolysis by spontaneously activated PDE

To estimate the rate of cGMP hydrolysis by a spontaneously activated PDE k_{sp}, we use the dark cGMP hydrolysis rate β_d and $\bar{P}^*_{sp,comp}$ and the relation [39, 1]

$$\beta_d = k_{sp} \bar{P}^*_{sp,comp}. \tag{7}$$

For a toad rod, the experimental value of β_d is not well known, and we found several values in the literature: $\beta_d = 0.1 s^{-1}$ [15], $\beta_d = 0.8 - 1.5 s^{-1}$ [23], $\beta_d = 1 s^{-1}$ [17]. For a salamander rod a value $\beta_d \sim 1^{-1}$ is mostly reported [41, 33, 42, 43, 44]. We used the median $\beta_d = 1 s^{-1}$ for our toad simulations shown in Fig. 1 in the main text and we investigated the effect of changing the value of β_d in section 6. For toad with $\beta_d = 1 s^{-1}$ and $\bar{P}^*_{sp,comp} = 1.25$ we find $k_{sp} \approx 0.8 s^{-1}$. For a mouse rod with $\beta_d = 4.1 s^{-1}$ [29] and $\bar{P}^*_{sp,comp} = 0.9$ (estimated in this work) we get $k_{sp} = 4.5 s^{-1}$. Thus, in both species cGMP hydrolysis by spontaneously activated PDE is not diffusion limited, and a spontaneously activated PDE enzyme is less efficient compared to a light-activated PDE. The different values of k_{sp} in toad and mouse might be due to the temperature, due to the different encounter rates between PDE and cGMP, or due to differences in the PDE enzyme between amphibians and mammals.

In summary, cGMP hydrolysis by light-activated PDE is diffusion limited and it occurs with a rate $k_{li} = k_{enc}$ computed from Eq. 6, whereas the hydrolysis rate k_{sp} from a spontaneously activated PDE is computed from Eq. 7 with values for β_d and $\bar{P}^*_{sp,comp}$.

Modeling cGMP dynamics

We shall now present our model for the number $G(n,t)$ of cGMP molecules in the nth compartment which can be obtained from the flux balance

$$\frac{\partial G(n,t)}{\partial t} = J_D(n,t) - J_H(n,t) + J_S(n,t) \tag{8}$$

where $J_S(n,t)$ is the local cGMP synthesis rate, $J_H(n,t)$ the hydrolysis rate due to spontaneously and light-activated PDE, and $J_D(n,t)$ is the diffusional flux between neighboring compartments. The molar cGMP concentration is $g(n,t) = \frac{G(n,t)}{\mathcal{N}_A V_{comp}}$, where $\mathcal{N}_A$ is the Avogadro constant and $V_{comp} \approx \pi R^2 h$ is the compartment volume where we neglect the small volume of the narrow gaps that connect adjacent compartments (Fig. S1). The cytosolic volume of the outer segment is $V_{os} = N_{comp} V_{comp}$.

We now explicitly evaluate Eq. 8:

1. cGMP synthesis is catalyzed by the enzyme guanylyl cyclase (GC) uniformly distributed on the surface of the disks. The synthesis rate depends on guanylyl cyclase activating proteins (GCAPs), that inhibit GC activity at high calcium concentration [45, 46, 47]. Because of the narrow compartments and the fast transversal diffusion, we can model cGMP synthesis as a uniform volume production rate:

$$J_S(n,t) = \mathcal{N}_A V_{comp} \alpha(n,t) = \mathcal{N}_A V_{comp} \frac{2\rho_{gc}}{h} \alpha_{max} \left(r_\alpha + (1-r_\alpha) \frac{K_\alpha^{n_\alpha}}{K_\alpha^{n_\alpha} + ca_f(n,t)^{n_\alpha}} \right), \tag{9}$$

where ρ_{gc} is the surface density of GC, α_{max} is the maximal synthesis rates attained at low free calcium concentrations, $r_\alpha = \frac{\alpha_{min}}{\alpha_{max}}$ is the ratio between the minimal and maximal synthesis rate, K_α is the calcium concentration for which the synthesis rate is $(\alpha_{max} + \alpha_{min})/2$, and n_α is the Hill coefficient. The value of K_α further depends on Mg^{2+} [46, 48, 49].

2. The rate of cGMP hydrolysis in a compartment is proportional to the number of spontaneously activated PDE $P_{sp}^*(n,t)$ and the number of light-activated PDE $P_{li}^*(n,t)$:

$$J_H(n,t) = \left(k_{sp} P_{sp}^*(n,t) + k_{li} P_{li}^*(n,t) \right) G(n,t) = \mathcal{N}_A V_{comp} \left(k_{sp} P_{sp}^*(n,t) + k_{li} P_{li}^*(n,t) \right) g(n,t). \tag{10}$$

3. The longitudinal cGMP diffusion between compartments generates fluxes with an effective longitudinal diffusion constant $D_{g,l} < D_g$, where D_g is the transversal cGMP diffusion constant [6]. The one-dimensional fluxes between neighboring compartments separated by the longitudinal distance $h + w$ (compartment height plus disk width) is approximated as

$$\begin{aligned} J_D(n,t) &\approx \mathcal{N}_A D_{g,l} \frac{\pi R^2 \left(g(n+1,t) + g(n-1,t) - 2g(n,t) \right)}{h+w} \\ &= \mathcal{N}_A V_{comp} \tilde{D}_{g,l} \left(g(n+1,t) + g(n-1,t) - 2g(n,t) \right), \end{aligned} \tag{11}$$

where the rate of diffusional exchange between neighboring compartments is

$$\tilde{D}_{g,l} = \frac{D_{g,l}}{h(h+w)}. \tag{12}$$

Finally, the equation for the molar cGMP concentration $g(n,t)$ is

$$\begin{aligned} \frac{d}{dt} g(n,t) &= \tilde{D}_{g,l} \left(g(n+1,t) + g(n-1,t) - 2g(n,t) \right) + \alpha(n,t) \\ &\quad - \left(k_{sp} P_{sp}^*(n,t) + k_{li} P_{li}^*(n,t) \right) g(n,t). \end{aligned} \tag{13}$$

6

Modeling calcium dynamics

To model Ca^{2+}-dynamics, we need to account for longitudinal diffusion between compartments, exchange between the OS and the extracellular medium through cGMP gated channels and $Ca^{2+}Na^+K^+$ exchangers, and buffering [50].

Calcium exchange through the membrane via channels and exchangers

Ca^{2+} ions are exchanged between the OS and the extracellular medium through cGMP gated channels and $Ca^{2+}Na^+K^+$ exchangers with fluxes $J_{ch,ca}(n,t)$ and $J_{ex,ca}(n,t)$, respectively. We use the convention that a flux of ions into the OS is positive, but the current defined by the inward flux of positive ions is negative.

The local calcium influx through the channel depends on the probability $p_{ch}(n,t)$ that a channel is open, which is a function of the local cGMP concentration:

$$p_{ch}(n,t) = \frac{g(n,t)^{n_{ch}}}{g(n,t)^{n_{ch}} + K_{ch}^{n_{ch}}} \,. \tag{14}$$

The calcium efflux through the exchanger depends on the local free calcium concentration $ca_f(n,t)$ and the exchanger saturation level:

$$p_{ex}(n,t) = \frac{ca_f(n,t)}{ca_f(n,t) + K_{ex}} \,. \tag{15}$$

The net local calcium flux $\Phi(n,t)$ through the membrane is

$$\Phi(n,t) = J_{ch,ca}(n,t) + J_{ex,ca}(n,t) = J_{ch,ca,max}p_{ch}(n,t) + J_{ex,ca,max}p_{ex}(n,t) \,. \tag{16}$$

We now relate $\Phi(n,t)$ to experimentally measured currents. The inward current through the channels carried by Na^+ and Ca^{2+} ions is

$$I_{ch}(n,t) = I_{ch,na}(n,t) + I_{ch,ca}(n,t) = \frac{I_{ch,ca}(n,t)}{f_{ca}} = -\frac{2e^+J_{ch,ca}(n,t)}{f_{ca}} \,, \tag{17}$$

where we used that the fraction $f_{ca} \sim 0.1 - 0.15$ of the current is carried by Ca^{2+} ions [32]. We have neglected the small contributions due to ions other than Na^+ and Ca^{2+} [51]). The extrusion of a single Ca^{2+} ion by the exchanger is accompanied by the influx of four Na^+ and the efflux of one K^+ [52]. Thus, the extrusion of one Ca^{2+} ion leads to the influx of a single positive charge, producing an exchanger current

$$I_{ex}(n,t) \quad = e^+J_{ex,ca}(n,t) \,. \tag{18}$$

From Eq. 17 and Eq. 18, the total local current is

$$I(n,t) = I_{ch}(n,t) + I_{ex}(n,t) = e^+\left(-\frac{2}{f_{ca}}J_{ch,ca}(n,t) + J_{ex,ca}(n,t)\right) \,. \tag{19}$$

At steady state in darkness, calcium influx and efflux balance one another, and we have $\langle J_{ex,ca}(n,t)\rangle_d + \langle J_{ch,ca}(n,t)\rangle_d = J_{ex,ca,comp,d} + J_{ch,ca,comp,d} = 0$. From Eq. 19 we obtain for the average dark current associated with a single compartment

$$I_{comp,d} = \langle I(n,t)\rangle_d = -e^+\left(\frac{2}{f_{ca}} + 1\right)J_{ch,ca,comp,d} = e^+\left(\frac{2}{f_{ca}} + 1\right)J_{ex,ca,comp,d} \,. \tag{20}$$

7

The calcium fluxes as a function of the current are

$$
\begin{aligned}
J_{ch,ca}(n,t) &= J_{ch,ca,comp,d}\frac{J_{ch,ca}(n,t)}{J_{ch,ca,comp,d}} = -\frac{I_{comp,d}}{e^{+}}\frac{f_{ca}}{f_{ca}+2}\frac{p_{ch}(n,t)}{p_{ch,d}} \\
J_{ex,ca}(n,t) &= J_{ex,ca,comp,d}\frac{J_{ex,ca}(n,t)}{J_{ex,ca,comp,d}} = \frac{I_{comp,d}}{e^{+}}\frac{f_{ca}}{f_{ca}+2}\frac{p_{ex}(n,t)}{p_{ex,d}},
\end{aligned}
\tag{21}
$$

with (g_d and ca_d are the mean steady state cGMP and calcium concentrations in darkness)

$$
p_{ch,d} = \frac{g_d^{n_{ch}}}{g_d^{n_{ch}}+K_{ch}^{n_{ch}}} \quad \text{and} \quad p_{ex,d} = \frac{ca_d}{ca_d+K_{ex}}.
\tag{22}
$$

By inserting these expressions into Eq. 16 we obtain

$$
\Phi(n,t) = \mathcal{N}_A V_{comp}\phi\left(\frac{p_{ch}(t)}{p_{ch,d}}-\frac{p_{ex}(t)}{p_{ex,d}}\right),
\tag{23}
$$

with the molar flux ($I_{os,d} = N_{comp}I_{comp,d}$, $V_{os} = N_{comp}V_{comp}$ and $\mathcal{F} = N_{Av}e^{+} = 9.65\times10^4 C/mol$ is the Faraday constant)

$$
\phi = \frac{f_{ca}}{f_{ca}+2}\frac{|I_{comp,d}|}{V_{comp}\mathcal{F}} = \frac{f_{ca}}{f_{ca}+2}\frac{|I_{os,d}|}{V_{os}\mathcal{F}}.
\tag{24}
$$

In a mouse rod, with a dark current $I_{os,d} = 16pA$ and a cytosolic volume $V_{os} = \pi R^2\frac{L}{2} \approx 18\mu m^3 = 18\times10^{-15}l$ [32], we estimate

$$
\phi \approx 500\frac{\mu M}{s} = 0.5\frac{\mu M}{ms}.
\tag{25}
$$

From the dark calcium concentration $ca_d \sim 0.3\mu M$ [32], we estimate that the dynamics of calcium exchange $\sim \frac{\phi}{ca_d}$ occurs at the time scale of a millisecond.

Finally, by inserting Eq. 21 into Eq. 19 we find that the local current is

$$
I(n,t) = I_{comp,d}\left(\frac{2}{f_{ca}+2}\frac{p_{ch}(n,t)}{p_{ch,d}}+\frac{f_{ca}}{f_{ca}+2}\frac{p_{ex}(n,t)}{p_{ex,d}}\right).
\tag{26}
$$

Calcium buffering

In darkness, a free calcium concentration $ca_d \approx 0.3\mu M$ [32] corresponds on average to ~ 3.3 free calcium ions in a compartment. Moreover, because the free calcium concentration decreases as a function of the light intensity, this is the maximum amount. Because adaptation and many other key phototransduction reactions are regulated by calcium [53], such a low number would be surprising unless most of the calcium in the OS is bound and buffered. Calcium buffering is due to several proteins: recoverin, guanylyl cyclase-activating proteins (GCAPs), and calmodulin. For example, the concentration of recoverin in a mammalian rod is $\sim 600\mu M$ [32], around 2000 times larger than the free calcium concentration; and the GC membrane concentration $\sim 50\mu m^{-2}$ [32] corresponds to ~ 150 enzymes in a mouse compartment, around 40 times more than the number of free calcium ions.

From the law of mass-action, the equation for the buffered calcium concentration $ca_b(n,t)$ is [18, 13]

$$
\frac{d}{dt}ca_b(n,t) = \alpha_b ca(n,t)(ca_{b_0}-ca_b(n,t))-\beta_b ca_b(n,t),
\tag{27}
$$

with ca_{b0} the total buffer concentration. On the assumption that the buffering reactions proceed rapidly in comparison to the rate of changes of the free calcium concentration, and that the total buffer concentration is much larger than the amount of buffered calcium ($ca_{b_0} \gg ca_b$), we can use the steady state solution of Eq. 27 to derive the relation

$$ca_b(n,t) = \frac{\alpha_b ca_{b_0}}{\beta_b} ca(n,t) = B_{ca} ca(n,t), \tag{28}$$

where the buffering capacity is $B_{ca} = \frac{\alpha_b ca_{b_0}}{\beta_b} = \frac{ca_b(n,t)}{ca_f(n,t)}$. In the absence of diffusion, the change in the total amount of calcium in a compartment is due to the inward and outward fluxes, that is

$$\mathcal{N}_A V_{comp} \frac{d}{dt}(ca_b(n,t) + ca(n,t)) = \Phi(n,t).$$

From Eq. 28 and Eq. 23 we obtain ($1 + B_{ca} \approx B_{ca}$)

$$\frac{d}{dt} ca(n,t) = \frac{\phi}{B_{ca}} \left(\frac{p_{ch}(t)}{p_{ch,d}} - \frac{p_{ex}(t)}{p_{ex,d}} \right) \tag{29}$$

Effective longitudinal diffusion of calcium

As for cGMP, we assume that longitudinal calcium diffusion proceeds with an effective diffusion constant $D_{ca,l}$. The rate of diffusional calcium exchange between neighboring compartments is then

$$\tilde{D}_{ca,l} = \frac{D_{ca,l}}{h(h+w)}. \tag{30}$$

By adding diffusional exchange to Eq. 29 we obtain a final equation

$$\frac{d}{dt} ca(n,t) = \tilde{D}_{ca,l}(ca(n+1,t) + ca(n-1,t) - 2ca(n,t)) + \frac{\phi}{B_{ca}} \left(\frac{p_{ch}(t)}{p_{ch,d}} - \frac{p_{ex}(t)}{p_{ex,d}} \right). \tag{31}$$

System of equations for cGMP, calcium and the current

With the steady state values given by g_d, ca_d, $\bar{P}_{sp,comp}^*$ and $I_{comp,d}$, we use the scaled quantities

$$\hat{g}(n,t) = \frac{g(n,t)}{g_d}, \quad \hat{ca}(n,t) = \frac{c(n,t)}{ca_d}, \quad \hat{P}_{sp}^*(n,t) = \frac{P_{sp}^*(n,t)}{\bar{P}_{sp,comp}^*},$$
$$\hat{I}(n,t) = \frac{I(n,t)}{I_{comp,d}} \quad \hat{I}_{os}(t) = \frac{I_{os}(t)}{I_{os,d}} \tag{32}$$
$$k_\alpha = \frac{K_\alpha}{ca_d}, \quad k_{ex} = \frac{K_{ex}}{ca_d}, \quad k_{ch} = \frac{K_{ch}}{g_d}.$$

The set of equations for the scaled variables are

$$\frac{d\hat{g}(n,t)}{dt} = \tilde{D}_{g,l}(\hat{g}(n+1,t) + \hat{g}(n-1,t) - 2\hat{g}(n,t)) + \beta_d \frac{r_\alpha + (1-r_\alpha)\frac{k_\alpha^{n_\alpha}}{k_\alpha^{n_\alpha} + \hat{ca}(n,t)^{n_\alpha}}}{r_\alpha + (1-r_\alpha)\frac{k_\alpha^{n_\alpha}}{k_\alpha^{n_\alpha} + 1}}$$
$$\qquad - \left(\beta_d \hat{P}_{sp}^*(n,t) + k_{li} P_{li}^*(n,t) \right) \hat{g}(n,t)$$
$$\frac{d\hat{ca}(n,t)}{dt} = \tilde{D}_{ca,l}(\hat{ca}(n+1,t) + \hat{ca}(n-1,t) - 2\hat{ca}(n,t)) + \gamma_d \left(\frac{p_{ch}(n,t)}{p_{ch,d}} - \frac{p_{ex}(n,t)}{p_{ex,d}} \right) \tag{33}$$
$$\hat{I}(n,t) = \frac{2}{f_{ca}+2} \frac{p_{ch}(n,t)}{p_{ch,d}} + \frac{f_{ca}}{f_{ca}+2} \frac{p_{ex}(n,t)}{p_{ex,d}}$$
$$\hat{I}_{os}(t) = \frac{1}{I_{os,d}} \sum_{n=1}^{N_{comp}} I(n,t) = \frac{1}{N_{comp}} \sum_{n=1}^{N_{comp}} \hat{I}(n,t)$$

9

where

$$
\begin{aligned}
\beta_d &= k_{sp}\bar{P}^*_{sp,comp} \\
\frac{p_{ch}(n,t)}{p_{ch,d}} &= \frac{1 + k_{ch}^{n_{ch}}}{\hat{g}(n,t)^{n_{ch}} + k_{ch}^{n_{ch}}}\hat{g}(n,t)^{n_{ch}} \\
\frac{p_{ex}(n,t)}{p_{ex,d}} &= \frac{1 + k_{ex}}{\hat{ca}(n,t) + k_{ex}}\hat{ca}(n,t) \,, \\
\gamma_d &= \frac{1}{B_{ca}}\frac{\phi}{ca_d} = \frac{1}{B_{ca}}\frac{f_{ca}}{f_{ca} + 2}\frac{|I_{os,d}|}{ca_d V_{os}\mathcal{F}} \,.
\end{aligned}
\tag{34}
$$

We further introduce the normalized currents

$$
\begin{aligned}
\hat{\mathcal{I}}(n,t) &= 1 - \hat{I}(n,t) \\
\hat{\mathcal{I}}_{os}(t) &= 1 - \hat{I}_{os}(t).
\end{aligned}
\tag{35}
$$

2 Analysis of the power spectrum and variance of the dark current

From a linear analysis of the equations we derived in the previous section, we now derive analytical expressions for the power spectrum. These expression will later be used to extract parameters from electrophysiological data.

Expressions for the power spectrum and variance of the dark current

By taking the Fourier transform and expanding expressions in Eq. 33 to first order in the absence of the photoresponse ($P^*_{li}(n,t) = 0$), we obtain the following system of equations

$$
\begin{aligned}
-i\omega\delta\hat{g}(n,\omega) &= \tilde{D}_{g,l}\left(\delta\hat{g}(n+1,\omega) + \delta\hat{g}(n-1,\omega) - 2\delta\hat{g}(n,\omega)\right) \\
&\quad + \beta_d\xi_\alpha\delta\hat{ca}(n,\omega) - \beta_d\delta\hat{g}(n,\omega) - \beta_d\delta\hat{P}^*_{sp}(n,\omega) \\
-i\omega\delta\hat{ca}(n,\omega) &= \tilde{D}_{ca,l}\left(\delta\hat{ca}(n+1,\omega) + \delta\hat{ca}(n-1,\omega) - 2\delta\hat{ca}(n,\omega)\right) \\
&\quad + \gamma_d\left(\xi_{ch}\delta\hat{g}(n,\omega) - \xi_{ex}\delta\hat{ca}(n,\omega)\right) \\
\delta\hat{I}(n,\omega) &= \frac{2}{f_{ca} + 2}\xi_{ch}\delta\hat{g}(n,\omega) + \frac{f_{ca}}{f_{ca} + 2}\xi_{ex}\delta\hat{ca}(n,\omega) \\
\delta\hat{I}_{os}(\omega) &= \frac{1}{N_{comp}}\left(\frac{2}{f_{ca} + 2}\xi_{ch}\delta\hat{g}(\omega) + \frac{f_{ca}}{f_{ca} + 2}\xi_{ex}\delta\hat{ca}(\omega)\right)
\end{aligned}
\tag{36}
$$

with

$$
\xi_\alpha = -n_\alpha\frac{1}{k_\alpha^{n_\alpha} + 1}\frac{(1 - r_\alpha)\frac{k_\alpha^{n_\alpha}}{k_\alpha^{n_\alpha}+1}}{r_\alpha + (1 - r_\alpha)\frac{k_\alpha^{n_\alpha}}{k_\alpha^{n_\alpha}+1}} \,, \quad \xi_{ch} = n_{ch}\frac{k_{ch}^{n_{ch}}}{1 + k_{ch}^{n_{ch}}} \,, \quad \xi_{ex} = \frac{k_{ex}}{1 + k_{ex}}
\tag{37}
$$

and

$$
\delta\hat{g}(\omega) = \sum_{n=1}^{N_{comp}}\delta\hat{g}(n,\omega) \,, \quad \delta\hat{ca}(\omega) = \sum_{n=1}^{N_{comp}}\delta\hat{ca}(n,\omega) \,.
\tag{38}
$$

By summing over the compartments, we obtain from the second term in Eq. 36

$$\delta \hat{c}a(\omega) = \frac{\gamma_d}{\gamma_d \xi_{ex} - i\omega} \xi_{ch} \delta \hat{g}(\omega) \,, \tag{39}$$

and by inserting this into the first term of Eq. 36 we get after summation

$$\delta \hat{g}(\omega) = \frac{\beta_d}{\beta_d - i\omega - \beta_d \xi_\alpha \frac{\gamma_d \xi_{ch}}{\gamma_d \xi_{ex} - i\omega}} \sum_{n=1}^{N_{comp}} \delta \hat{P}_{sp}^*(n, \omega) \,. \tag{40}$$

Finally, with the last expression in 36, the overall current fluctuation depends on the spontaneous PDE fluctuation by the relation

$$\begin{aligned}
\delta \hat{I}_{os}(\omega) &= \frac{1}{N_{comp}} \left(\frac{2}{f_{ca} + 2} + \frac{f_{ca}}{f_{ca} + 2} \frac{\gamma_d \xi_{ex}}{\gamma_d \xi_{ex} - i\omega} \right) \xi_{ch} \delta \hat{g}(\omega) \\
&= \chi_I(\omega) \frac{1}{N_{comp}} \sum_{n=1}^{N_{comp}} \delta \hat{P}_{sp}^*(n, \omega)
\end{aligned} \tag{41}$$

with the transfer function

$$\begin{aligned}
\chi_I(\omega) &= \left(1 + \frac{f_{ca}}{f_{ca} + 2} \frac{i\omega}{\gamma_d \xi_{ex} - i\omega} \right) \frac{\xi_{ch} \beta_d}{\beta_d \left(1 - \frac{\gamma_d^2 \xi_\alpha \xi_{ch} \xi_{ex}}{\gamma_d^2 \xi_{ex}^2 + \omega^2} \right) - i\omega \left(1 + \frac{\beta_d \gamma_d \xi_\alpha \xi_{ch}}{\gamma_d^2 \xi_{ex}^2 + \omega^2} \right)} \\
&\approx -\frac{\xi_{ch} \beta_d}{\beta_d \left(1 - \frac{\gamma_d^2 \xi_\alpha \xi_{ch} \xi_{ex}}{\gamma_d^2 \xi_{ex}^2 + \omega^2} \right) - i\omega \left(1 + \frac{\beta_d \gamma_d \xi_\alpha \xi_{ch}}{\gamma_d^2 \xi_{ex}^2 + \omega^2} \right)}
\end{aligned} \tag{42}$$

Because the activation of PDE in a compartment occurs independently of other compartments, the spectrum of the overall scaled current $\hat{I}_{os}(t)$ is ($P_{sp,os}^* = N_{comp} \bar{P}_{sp,comp}^*$)

$$S_{\hat{I}_{os}}(\omega) = |\chi_I(\omega)|^2 \frac{1}{N_{comp}} \hat{S}_{P_{sp}^*} = \frac{1}{N_{comp}} \frac{|\chi_I(\omega)|^2}{P_{sp,comp}^*} \frac{4\mu_{sp}}{\mu_{sp}^2 + \omega^2} = \frac{|\chi_I(\omega)|^2}{P_{sp,os}^*} \frac{4\mu_{sp}}{\mu_{sp}^2 + \omega^2} \,. \tag{43}$$

The variance of the scaled current is

$$\Sigma_{\hat{I}_{os}}^2 = \frac{1}{2\pi} \int_0^\infty S_{\hat{I}_{os}}(\omega) d\omega \,. \tag{44}$$

The power spectrum scaled by the current variance

$$\hat{S}_{\hat{I}_{os}}(\omega) = \frac{S_{\hat{I}_{os}}(\omega)}{\Sigma_{\hat{I}_{os}}^2} \tag{45}$$

is independent of the number of spontaneously activated PDE.

Analytic expressions for the power spectrum and variance of the dark current in a GCAPs$^{-/-}$ rod

In a GCAPs$^{-/-}$ rod, cGMP synthesis is not calcium dependent and thus $\xi_\alpha = 0$ (Eq. 37). In this case the transfer function $\chi_I(\omega)$ in Eq. 42 reduces to

$$\chi_I(\omega) = -\frac{\xi_{ch} \beta_d}{\beta_d - i\omega} \tag{46}$$

11

and the spectrum and variance of the overall scaled current are

$$S_{\hat{I}_{os},gcap}(\omega) = \frac{4\xi_{ch}^2}{\bar{P}_{sp,os}^* \mu_{sp}} \frac{\beta_d^2 \mu_{sp}^2}{(\beta_d^2 + \omega^2)(\mu_{sp}^2 + \omega^2)} \tag{47}$$

$$\Sigma_{\hat{I}_{os},gcap}^2 = \frac{\xi_{ch}^2}{\bar{P}_{sp,os}^*} \frac{1}{1 + \frac{\mu_{sp}}{\beta_d}} = \frac{\xi_{ch}^2}{N_{comp}\bar{P}_{sp,comp}^*} \frac{1}{1 + \frac{\mu_{sp}}{\beta_d}} . \tag{48}$$

From the mouse parameter values in Table S4, we compute $\Sigma_{\hat{I}_{os},gcap} \approx 0.055$, which agrees well with the value 0.056 extracted from the GCAPs$^{-/-}$ simulations shown in Fig. 2 in the main text.

The spectrum scaled by the variance depends only on β_d and μ_{sp},

$$\hat{S}_{\hat{I}_{os}}(\omega) = 4 \frac{(\beta_d + \mu_{sp}) \beta_d \mu_{sp}}{(\beta_d^2 + \omega^2)(\mu_{sp}^2 + \omega^2)} \tag{49}$$

Analytic expressions for the power spectrum and variance of the dark current with fast calcium dynamics

In general, it is difficult to derive explicit expressions for the power spectrum and the current variance from Eq. 43 and Eq. 44 with calcium feedback. However, as will be shown now, provided the rate of calcium change is sufficiently rapid, we can obtain analytical formulas for the power spectrum and the variance of the dark current which can be compared to the case of GCAPs$^{-/-}$ with no calcium feedback. Negative calcium feedback on cGMP synthesis reduces the current variance and is most efficient when the rate of change of calcium is fast compared to PDE fluctuations. Such considerations make it possible to estimate the maximal effect of calcium feedback on the variance of the current.

In a mouse rod without buffering, the change in calcium in Eq. 33 proceeds with a fast rate of $\gamma_d \approx 1670 s^{-1}$ (Eq. 34 with $B_{ca} = 1$ and other parameter values from Table S4). Buffering ($B_{ca} > 1$) slows down the dynamics and reduces the feedback. For $\omega \ll \gamma_d \xi_{ex}$ Eq. 42 simplifies to

$$\chi_I(\omega) \approx -\frac{1}{\zeta} \frac{\xi_{ch} \tilde{\beta}_d}{\tilde{\beta}_d - i\omega} \tag{50}$$

with

$$\zeta = 1 - \frac{\xi_\alpha \xi_{ch}}{\xi_{ex}}, \quad \tilde{\beta}_d = \beta_d \zeta \frac{1}{1 - \frac{\beta_d(\zeta - 1)}{\gamma_d \xi_{ex}}} . \tag{51}$$

The spectrum and variance of the dark current are

$$S_{\hat{I}_{os},fastCa}(\omega) = \frac{1}{\zeta^2} \frac{4\xi_{ch}^2}{\bar{P}_{sp,os}^* \mu_{sp}} \frac{\tilde{\beta}_d^2 \mu_{sp}^2}{(\tilde{\beta}_d^2 + \omega^2)(\mu_{sp}^2 + \omega^2)} \tag{52}$$

$$\Sigma_{\hat{I}_{os},fastCa}^2 = \frac{1}{\zeta^2} \frac{\xi_{ch}^2}{\bar{P}_{sp,os}^*} \frac{1}{1 + \frac{\mu_{sp}}{\tilde{\beta}_d}} . \tag{53}$$

The spectrum scaled by the variance depends on μ_{sp} and $\tilde{\beta}_d$ and

$$\hat{S}_{\hat{I}_{os},fastCa}(\omega) = 4 \frac{\left(\tilde{\beta}_d + \mu_{sp}\right) \tilde{\beta}_d \mu_{sp}}{(\tilde{\beta}_d^2 + \omega^2)(\mu_{sp}^2 + \omega^2)} . \tag{54}$$

Compared to GCAPs$^{-/-}$ rods, calcium feedback reduces the standard deviation of the dark current by a factor

$$\frac{\Sigma_{\hat{I}_{os},gcap}}{\Sigma_{\hat{I}_{os}fastCa}} = \zeta \sqrt{\frac{1 + \frac{\mu_{sp}}{\tilde{\beta}_d}}{1 + \frac{\mu_{sp}}{\beta_d}}} \,. \tag{55}$$

With the parameters given in Table S4 (with $B_{ca} = 80$ and $r_\alpha = 0.066$) we compute $\zeta = 4.7$, $\tilde{\beta}_d \approx 86 s^{-1}$ and

$$\frac{\Sigma_{\hat{I}_{os},gcap}}{\Sigma_{\hat{I}_{os}fastCa}} \approx 2.5 \,. \tag{56}$$

From the experimental data and the dark current simulations shown in Fig. 2 and 3 in the main text, we find a ratio $\sim 0.056/0.023 \approx 2.4$, in good agreement with the above theoretical estimation. Calcium feedback is maximal when there is no buffering ($B_{ca} = 1$) and when cGMP synthesis is affected also at a high free calcium concentration in darkness ($r_\alpha = 0$, see Eq. 33). With $B_{ca} = 1$ and $r_\alpha = 0$ we get $\zeta \approx 7.4$, $\tilde{\beta}_d \approx 31 s^{-1}$ and

$$\frac{\Sigma_{\hat{I}_{os},gcap}}{\Sigma_{\hat{I}_{os}fastCa}} \approx 4.4 \,. \tag{57}$$

In summary, by comparing Eq. 48 with Eq. 53, we conclude that calcium feedback reduces the current variance due to a global factor ζ and due to increasing the value of β_d to an effective value $\tilde{\beta}_d$. This increase in β_d is also responsible for the faster dynamics of the single-photon response in wild type compared to GCAPs$^{-/-}$ mice.

3   Simulation Protocol

We now briefly describe our simulation method. For each compartment, we use the Gillespie algorithm [14] to generate independent spontaneously activated PDE $P_{sp}^*(n,t)$ from Poisson activation and deactivation rates ν_{sp} and μ_{sp}. To model the single-photon response, we simulated the number of light-activated PDE $P_{li}^*(t)$ in the compartment where the photon is absorbed. For simplicity, we assume that the photon is absorbed at the center of the outer segment. However, a different location would not have a significant effect on the results. Finally, with $P_{sp}^*(n,t)$ and $P_{li}^*(t)$ as input functions, we integrated the system of equations for calcium and cGMP (Eq. 33) and obtained the local currents $\hat{I}(n,t)$ and the overall current $\hat{I}_{os}(t)$. Finally, we computed the normalized currents $\hat{\mathcal{I}}(n,t) = 1 - \hat{I}(n,t)$ and $\hat{\mathcal{I}}_{os}(t) = 1 - \hat{I}_{os}(t)$.

4   Data analysis and parameter extraction

We analyzed experimental recordings of dark currents in wild type (WT) and GCAPs$^{-/-}$ knockout mice and used our expressions for the power spectrum and variance to extract unknown parameters.

Extraction of μ_{sp} and $P_{sp,comp}^*$ from current recordings in GCAPs$^{-/-}$ knockout mice

In GCAPs$^{-/-}$ knockout mice, the power spectrum of the dark current scaled by the variance reduces to a double Lorentzian given by Eq. 49 and depends only on the parameters μ_{sp} and β_d. We first

tried to use Eq. 49 as a function of ω to extract μ_{sp} and β_d by fitting current recordings obtained from GCAPs$^{-/-}$ knockout mice. Unfortunately, it is not possible to fit both parameters μ_{sp} and β_d reliably at the same time, because distinct pairs (μ_{sp}, β_d) result in very similar curves (see Fig S3c). However, because $\beta = 4.1s^{-1}$ [29] has been recently estimated for a mouse rod, we used this value in Eq. 49 and fitted only the unknown parameter μ_{sp}, which gave reliable results.

To compute μ_{sp} we proceeded as follows. We acquired current recordings from 15 rods in darkness and in bright light to estimate the dark and instrumental noise. We filtered currents at 20Hz, and because instrumental and dark noise are independent, we computed for each rod the dark noise power spectrum by subtracting the power spectrum of the instrumental noise from the power spectrum of the recordings in darkness [15]. We then scaled for each rod the dark noise power spectrum with the corresponding dark-light current variance. Finally we used Eq. 49 within the frequency range 0.1-5Hz to fit for each rod an individual value μ_{sp}. From recordings of 15 rods, we obtained $\mu_{sp} = 12.0 \pm 3.7s^{-1}$. The large variability is the result of noisiness in the power spectra (Fig S3a), in part the result of the relatively short duration (between 5 and 15 seconds) of patch-clamp current recordings from individual rods.

To obtain a longer current trace, we first normalized the currents for each rod and then concatenated these individual normalized currents. For each rod, we scaled the dark and light currents with the standard deviation dark-light and then concatenated these normalized dark and light currents. From this much longer current trace, we computed the dark-light power spectrum (Fig S3b), and by fitting this spectrum we obtained $\mu_{sp} = 12.8s^{-1}$, which is close to the mean value obtained from individual rod spectra. For the simulations in the main text, we used the interpolated value $\mu_{sp} = 12.4s^{-1}$. The analytic curve in Fig S3a,b computed with $\mu_{sp} = 12.4s^{-1}$ and $\beta = 4.1s^{-1}$ is added to show the agreement with the data.

Next, from the values of μ_{sp} and β_d we estimated the mean number of spontaneously activated PDE per compartment $\bar{P}_{sp,comp}^*$ from the expression for the scaled current variance given in Eq. 48 (we use $N_{comp} = 810$). We computed for each rod the dark-light variance of the current recordings scaled by the dark current, and then used μ_{sp} estimated for that rod to compute $\bar{P}_{sp,comp}^*$. With this procedure, we obtained $\bar{P}_{sp,comp}^* = 0.9 \pm 0.42$. From the concatenated scaled current we computed $\bar{P}_{sp,comp}^* = 0.94$. For the simulations in the main text we used $\bar{P}_{sp,comp}^* = 0.9$.

Extraction of r_α and B_{ca} from current recordings in WT mice

We utilized $\beta = 4.1s^{-1}$ and $\mu_{sp} = 12.4s^{-1}$ to compute the power spectrum for WT rods from Eq. 43 and compared it with experimental observations. For WT rods, the dark noise additionally depends on calcium feedback. The standard deviation of the WT dark noise amplitude is reduced by a factor around 2-2.5 (see Fig. 2 and 3 in the main text) compared to the GCAPs$^{-/-}$ value, which is less than a factor of 4.4 predicted for maximal calcium feedback. As discussed previously, the the amount of calcium feedback depends significantly on the values for r_α and B_{ca}, which are both not precisely known. In most models $r_\alpha = 0$ is assumed [54, 18, 32], in [25] a value of $r_\alpha = 0.072$ is used, which is is also in the range of what is suggested by experimental recordings [46, 48]. In [32, 54] a buffering capacity $B_{ca} = 50$ is assumed, and $B_{ca} = 20$ is used in [25]. In [18] it was assumed that $\sim 300\mu M$ calcium was buffered in the dark, corresponding to $B_{ca} \sim 100$.

To clarify the values of r_α and B_{ca}, we decided to use the dark-light power spectrum derived from recordings in WT mice and fit r_α and γ_d from Eq. 43. From the fitted value for γ_d, we computed B_{ca} from Eq. 34. In WT mice the separation between physiological and instrumental noise is much less compared to GCAPs$^{-/-}$ knockout mice, which resulted in much noisier individual spectra (Fig. S4b).
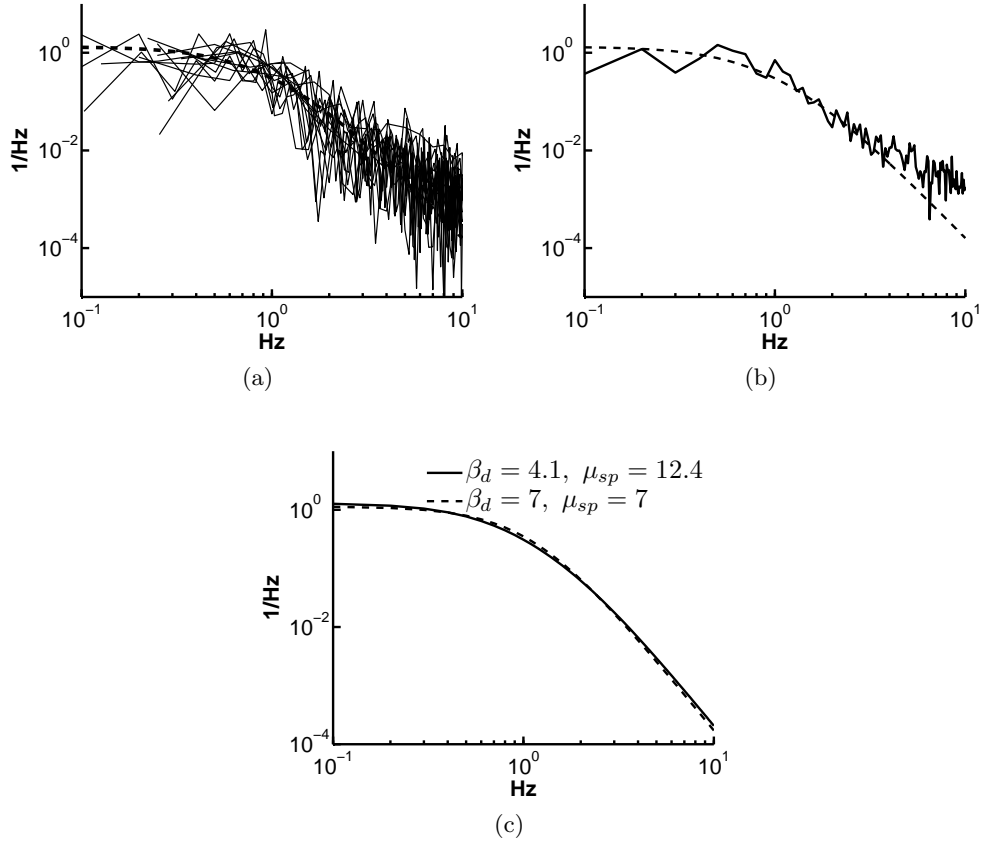
(a)

(b)

(c)

Fig. S3: **Dark-light power spectrum scaled by the variance for GCAP$^{-/-}$ mouse rod**. (a) Superposition of 15 dark-light power spectra scaled by the variance dark-light obtained from current recordings from 15 rods from GCAPs$^{-/-}$ knockout mice. The dashed line is computed from Eq. 49 with $\beta = 4.1s^{-1}$ and $\mu_{sp} = 12.4s^{-1}$. (b) Dark-light power spectrum obtained from the normalized currents that were concatenated. The dashed line is the same as in (a). (c) The curves are computed from Eq. 49 with β and μ_{sp} as indicated in the legend.
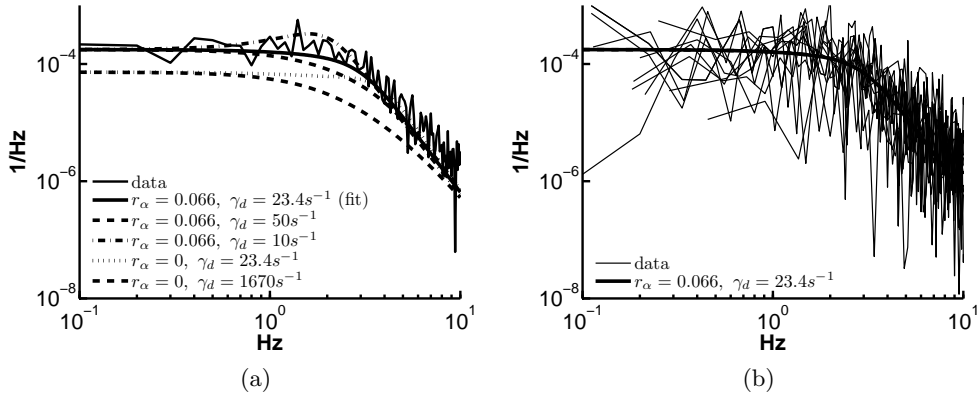
Fig. S4: **Dark-light power spectrum for WT mouse rod**. (a) The experimental dark-light power spectrum is computed from the scaled currents of 11 rods that were subsequently concatenated. The best fit from Eq. 43 is obtained for $r_\alpha = 0.06$ and $\gamma_d = 23.4$ (with $\beta = 4.1 s^{-1}$ and $\mu_{sp} = 12.4 s^{-1}$). The additional curves show the analytic spectrum for various r_α and γ_d. (b) The experimental dark-light power spectra for each rod. The analytic curve is the best fit from (a).

Unfortunately, we could not reliably fit r_α and γ_d separately for each rod from these individual power spectra. Nevertheless, to obtain an estimation for r_α and γ_d, we concatenated the scaled currents from the 11 rods and computed the less noisy dark-light spectrum shown in Fig. S4. By fitting this spectrum with Eq. 43, we obtained $r_\alpha = 0.066$ and $\gamma_d = 23.4 s^{-1}$. In Fig. S4a we additionally show how the analytic spectrum changes by varying r_α and γ_d, and in Fig. S4b we compare the analytic spectrum with the individual spectra. From the measured mean dark current of 17.9pA, we computed $B_{ca} = 80$ from Eq. 34.

5 Single-photon response simulations and calcium feedback for mouse rod

We combined our previous analysis and simulated the normalized dark current and single-photon response (Fig. S5a). The variability of the response (Fig. S5e) arises from fluctuations in the number of spontaneous and light-activated PDE; however, experimentally, it is very difficult to separate the impact of these two noise sources. We therefore used our approach to dissect their contributions by performing simulations with noise due only to spontaneous PDE activation or due only to light-activated PDE.

When noise is generated exclusively by spontaneous PDE activation (Fig. S5b), we expect that, to a first approximation, the variance is time independent and equals the variance of the dark noise (we found $\Sigma_{dark} \approx 0.023$, see Fig. 3 in the main text). Fig. S5e shows that this general view is only partly correct, and we surprisingly found a decrease in the standard deviation around time to peak to a value of $\Sigma_{dark} \approx 0.018$. We checked that this result is not simply a statistical fluctuation by performing additional simulations that gave similar results. The reduced variance around time to peak is probably related to the decrease in the cGMP concentration when the number of light-activated PDE increases. However, a more precise analysis has to be performed in future work.

Next we performed simulations without dark noise (Fig. S5c) where the variability (Fig. S5f) is

16

only due to fluctuations in the number of light-activated PDE. The standard deviation of the peak current extracted from the simulations is $\Sigma_{peak} \approx 0.028$. We noted that the noise at peak time in Fig. S5a is not simply the sum of the noise from spontaneous and light-activated PDE because $\sqrt{(0.018^2 + 0.028^2)} \approx 0.033$ is around 10% larger than the value of 0.030 in Fig. S5d. Similar to what we found about the reduction in the variance at time to peak in Fig. S5e, this result confirms the coupling of the effects of spontaneous and light-activated PDE with the cGMP concentration, which therefore cannot be independent. With 0.072 for the mean peak amplitude, we compute that the coefficient of variation (CV, ratio of mean to standard deviation) of the peak current amplitude in Fig. S5c is $CV_{peak} = 0.028/0.072 \approx 0.39$. We compared this value to the CV of the peak number of light-activated PDE ($CV_{P^*_{li,max}}$). As shown in [16], $CV_{P^*_{li,max}}$ strongly depends on whether R^* or PDE deactivation limits the photoresponse recovery, and the coefficient of variation of R^* lifetime ($CV_{\tau_{rh}}$) is in general not a good estimate for $CV_{P^*_{li,max}}$. In a toad rod, where rhodopsin deactivation is rate limiting, we find $CV_{P^*_{li,max}} \approx 0.19$ (see Fig 1A in the main text), much lower than the minimum value $1/\sqrt{N_p + 1} \approx 0.37$ for $CV_{\tau_{rh}}$ [16]. In mouse, where rhodopsin deactivation occurs much faster than the deactivation of a light-activated PDE, we can use Eq.43 from [16] with $N = N_p + 1 = 7$ and $\bar{P}^*_{li,max} = 8.2$ to approximate

$$CV_{P^*_{li,max}} \approx \sqrt{\frac{1 + \frac{N}{\bar{P}^*_{li,max}}}{N}} \approx 0.51 \,, \tag{58}$$

in agreement with $CV_{P^*_{li,max}} \approx 0.49$ extracted from the simulations shown in Fig. 4C in the main text. Furthermore, when rhodopsin deactivation is faster than PDE deactivation, it was shown in [16] that the PDE variance peaks around the same time as the PDE mean, and Fig. S5f shows that this is also true for the current. Moreover, the time course of the current variance closely follows that of the mean. In contrast, when PDE deactivation is faster than rhodopsin deactivation, the variance peaks later than the mean [16, 22].

We were then interested to know whether the reduction from $CV_{P^*_{li,max}} \approx 0.51$ to $CV_{peak} \approx 0.39$ is due to negative calcium feedback affecting cGMP synthesis. To resolve this question, we performed simulations without dark noise for a GCAPs$^{-/-}$ rod without calcium feedback (Fig. S6a) and for a situation with increased calcium feedback ($B_{ca} = 1$ and $r_\alpha = 0$) (Fig. S6b). Calcium feedback indeed reduces the standard deviation of the peak current from a value $\Sigma_{peak} \approx 0.053$ in a GCAPs$^{-/-}$ rod by a factor around 3.3 to a value $\Sigma_{peak} \approx 0.016$ with increased feedback (Fig. S6c,d), similar to the factor 4.4 computed for the reduction of the standard deviation of the dark noise in Eq. 57. At the same time, however,the peak current amplitude is also reduced by a factor around 3.6 from 0.14 to 0.039, such that the CV of the peak current remains almost unchanged, $CV_{peak} = 0.053/0.14 \approx 0.38$ and $CV_{peak} = 0.016/0.039 \approx 0.41$. This shows that the lower CV of the peak current amplitude compared to light-activated PDE is not due to calcium feedback but due to intrinsic properties of Eqs. 33. To conclude, because calcium feedback reduces both the fluctuations and the photoresponse peak amplitude by a similar factor, it does not increase the fidelity of the single-photon response amplitude, in agreement with [22, 24] but different from the result published in [54].

Finally, in Fig. S7 and in Fig. 5 in the main text we present simulations that reveal how important adaptations between the biochemistry and the geometry are in order to preserve the fidelity of a single-photon response. In Fig. 5A in the main text we show that the SPR is lost in the background noise if the PDE density and the ratio ν_{sp}/μ_{sp} are the same in mouse and toad rods, leading to $\bar{P}^*_{sp,comp} = 0.08$ in a mouse rod. If a spontaneous activated PDE has the hydrolytic activity of a light-activated PDE, $k_{sp} = k_{li} = 61s^{-1}$, a value $\bar{P}^*_{sp,comp} = 0.9$ results in $\beta_d \approx 55s^{-1}$, in which case 8 light-activated PDE are not enough to produce a noticeable single-photon response (Fig. S7).
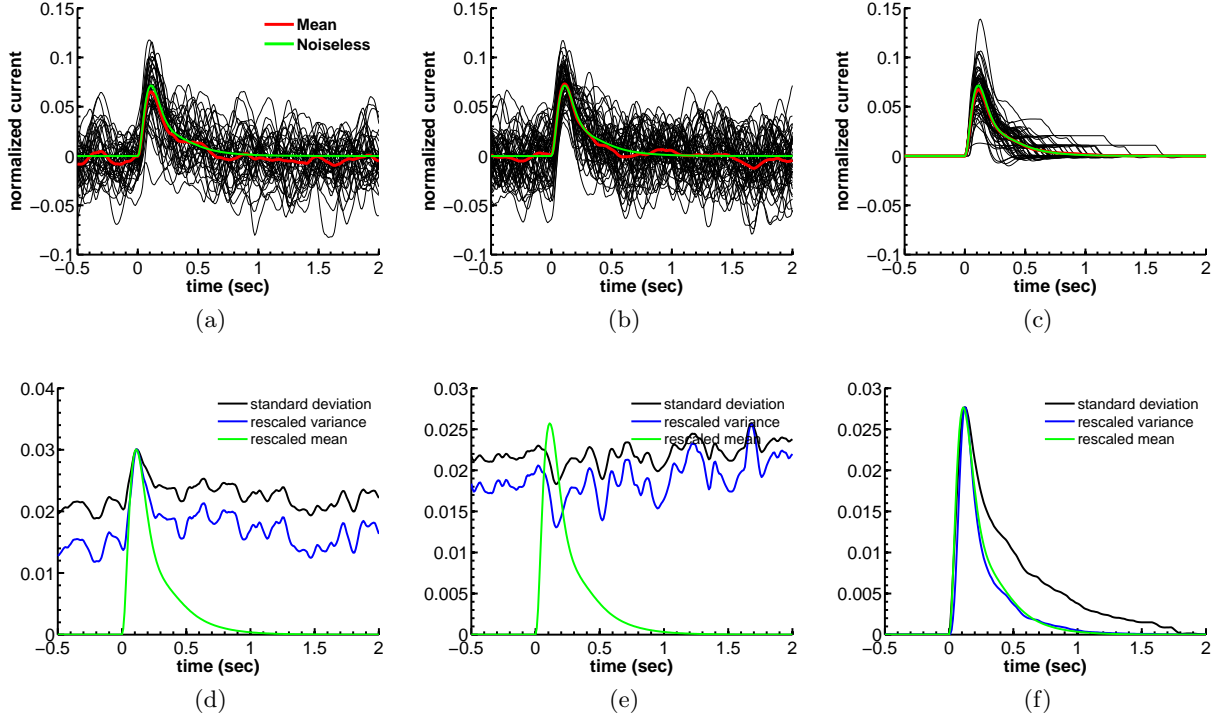
Fig. S5: **Single-photon response simulations for WT mouse.** (a) Superposition of the normalized currents $\hat{\mathcal{I}}_{os}(t) = 1 - \hat{I}_{os}(t)$ from 50 SPR simulations (black) with mean (red) and with a noiseless simulation of the mean (green). The noiseless simulation (shown in all panels) is obtained from the mean number of spontaneously activated PDE per compartment and from the analytic curve for the mean number of light-activated PDE computed with equations from [16] (see Fig. 1A and Fig. 4C in the main text). Time to peak and peak amplitude of the noiseless simulation are 110ms and 0.072. (b) Superposition of 50 simulations with noise from spontaneous PDE only. (c) Superposition of 50 simulations with noise from light-activated PDE only. (d) Time dependent standard deviation computed from the simulations in (a). We further show the rescaled variance and the rescaled noiseless simulation to compare the time courses (we rescaled such that the maximal values agree). The standard deviation of the peak current is $\Sigma_{peak} \approx 0.030$. (e) Time dependent standard deviation computed from the simulations in (b). The standard deviation near the peak of the current is reduced to $\Sigma_{peak} \approx 0.018$. (f) Time dependent standard deviation computed from the simulations in (c). The standard deviation at the peak is $\Sigma_{peak} \approx 0.028$. Parameters are from Tables S3,S4
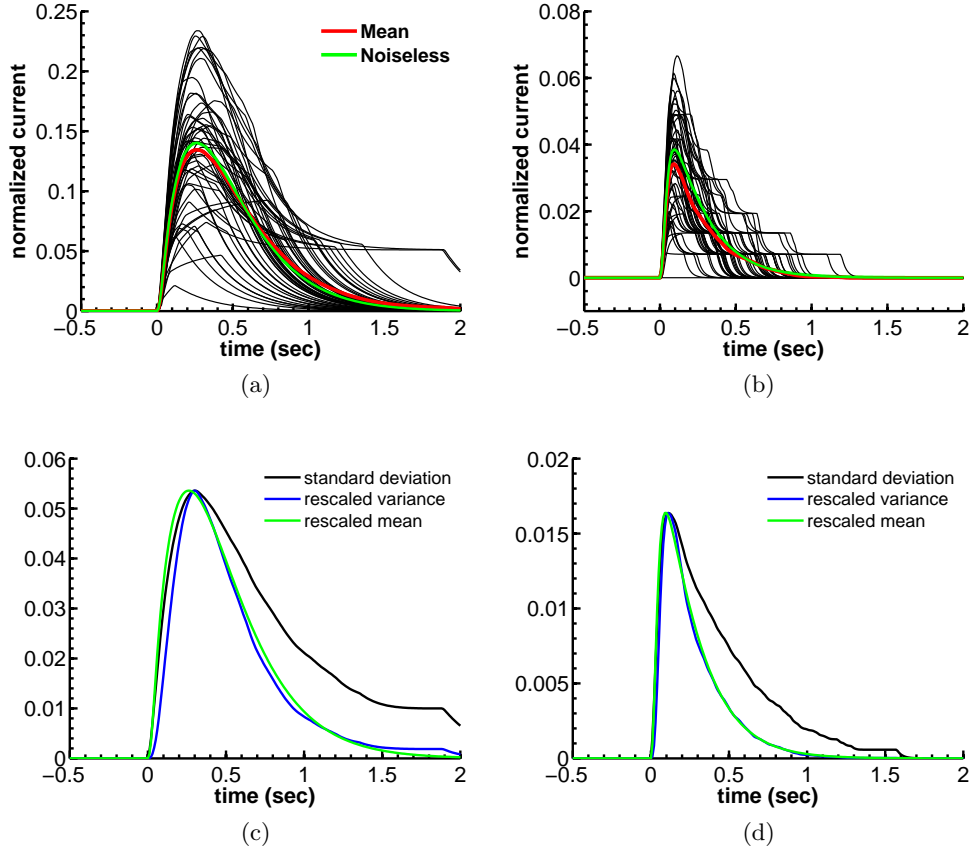
Fig. S6: **Single-photon response simulations for mouse rod without dark noise.** (a) Superposition of 50 simulations for GCAPs$^{-/-}$ rod with no calcium feedback. Time to peak and peak amplitude of the noiseless simulation are 270ms and 0.14. (b) Superposition of 50 simulations for a rod with strong calcium feedback ($B_{ca} = 1$ and $r_\alpha = 0$). Time to peak and peak amplitude of the noiseless simulation are 100ms and 0.039. (c-d) Time dependent standard deviations computed from the simulations in (a-b). The rescaled time courses of the variance and the noiseless mean simulation from (a-b) are shown for comparison. The peak standard deviations in (c-d) are $\Sigma_{peak} \approx 0.053$ and $\Sigma_{peak} \approx 0.016$ respectively.
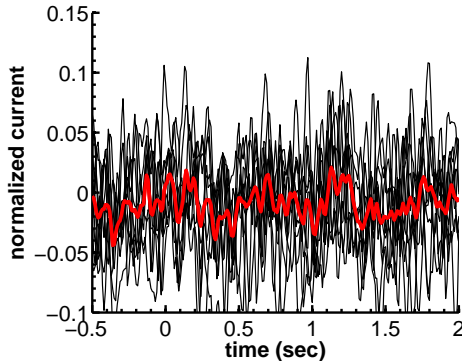
Fig. S7: **Single-photon response simulations for mouse rod with $k_{sp} = k_{li}$.** Superposition of 10 simulations with a single-photon absorption at time t=0s when spontaneous and light-activated PDEs have the same hydrolytic activity, $k_{sp} = k_{li} = 61s^{-1}$ leading to $\beta_d \approx 55s^{-1}$ with $\bar{P}^*_{sp,comp} = 0.9$. All other parameters are as in Tables S3,S4.

6 Effect of calcium feedback and the value of β_d on the single-photon response in a toad rod

Because there is uncertainty in the literature about the value of β_d for a toad rod, we performed single-photon response simulations with $\beta_d = 0.5s^{-1}$ (Fig. S8) to estimate the effect of a reduced value of β_d. Surprisingly, with $\beta_d = 0.5s^{-1}$ only around 60 light-activated PDEs are needed (Fig. S8a) to reduce the current by around 5% (Fig. S8b). The simulations in Fig. S8b with $\beta_d = 0.5s^{-1}$ and 60 light-activated PDEs are almost indistinguishable from the simulations shown in Fig. 1B in the main text generated with $\beta_d = 1s^{-1}$ and 150 light-activated PDEs. The reduction in β_d does not slow down the dynamics because rhodopsin and PDE deactivation proceed at a similar time scale.

Next we analyzed the impact of calcium buffering. In a toad rod, a buffering capacity $B_{ca} = 80$ as estimated for mouse rod would reduce the rate γ_d (Eq. 34) from $92s^{-1}$ to around $1s^{-1}$, which would inappropriately alter the dynamics of the photonresponse (Fig. S9a). For salamander, a much lower a calcium buffering capacity around 20 is found [33], and $B_{ca} = 20$ is used for the modeling in [20]. However, if the assumption o fast calcium binding dynamics would not not justified in amphibians, the simplified model with an effective parameter B_{ca} would not be appropriate, and the calcium binding reactions would have to be modeled explicitly [17, 18].

We do not have experimental recordings from toad rods which we could use to (1) validate whether a model with an effective parameter B_{ca} is justified, and (2), to estimate the values of B_{ca} and r_α. We therefore used the generic parameters $B_{ca} = 1$ and $r_\alpha = 0$ for the simulations shown in Fig1B in the main text, and obtained good agreement with experimental recordings [23]. Nevertheless, we present here additional simulations where we modify the calcium dynamics in Fig. S9 to establish whether the conclusions in the main text are affected by changing the values for B_{ca} and r_α.

Increasing the buffering capacity up to a value of $B_{ca} = 20$ does not much alter the photon response (Fig. S9a,b). In contrast, with a value of $r_\alpha = 0.066$ both amplitude of the photon response and the dark noise level increase by a factor of about 1.5 (Fig. S9c). Thus, with $r_\alpha = 0.066$, around 100 light-activated PDE would induce the same amplitude as 150 light-activated PDE in the case with $r_\alpha = 0$. Other quantities like standard deviation or the CV are little affected.
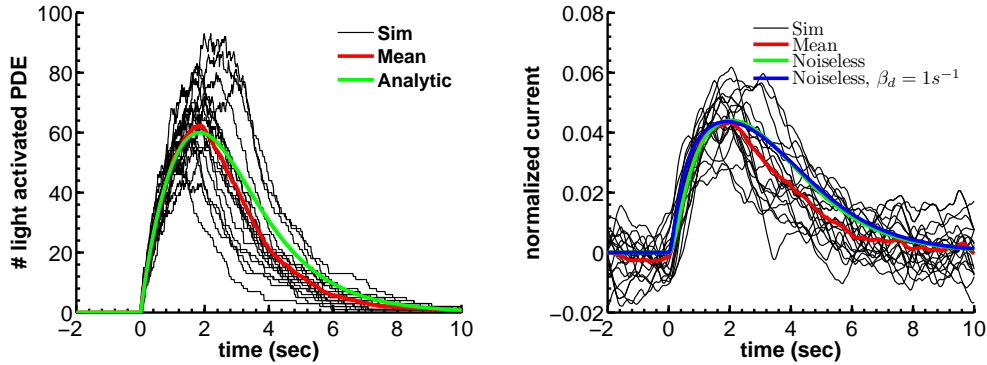
Fig. S8: **Simulation of dark noise and single-photon response for a toad rod with $\beta_d = 0.5s^{-1}$ and $\gamma_{rt,max} = 80s^{-1}$.** (A) Superposition of 20 simulations (black) of the time course for the number of light-activated PDE after a photon absorption. The mean is red and the analytic curve for the mean is green. Time to peak and peak value of the analytic curve are 1.85 sec and 60. The coefficient of variation (CV) extracted from the simulations is around 0.23.(B) Superposition of 20 single-photon response simulations (black, normalized current) obtained with the light-activated PDE shown in (A). The mean is red, and the noiseless simulation (green) is obtained without spontaneous PDE noise and with the analytic curve for light-activated PDE from (A). The noiseless simulation from Fig. 1B in the main text (blue) is also superimposed for comparison. Time to peak and peak amplitude of the noiseless simulation are around 2 sec and 0.044. The standard deviation of the dark noise and the CV of the peak amplitude extracted from the simulations are around 0.007 and 0.22. Except for β_d and $\gamma_{rt,max}$, all parameters are given in Table S3 and S4.

7 Impact of longitudinal cGMP diffusion on the single-photon response in a mouse rod

Because there is uncertainty about the effect and value of the cGMP longitudinal diffusion constant in rods (see for example [29, 44], we decided to run simulations to test how the background noise and the single-photon response is affected by a change in this constant. In Fig. S10 we show simulations of a single-photon absorption in a mouse rod with various longitudinal cGMP diffusion constants $D_{g,l} = 0, 2, 10, 40 \frac{\mu m^2}{s}$. The upper panels show the normalized current $\hat{\mathcal{I}}(n,t) = 1 - \hat{I}(n,t)$ in the compartment where the photon is absorbed, and the lower panels show the normalized overall current $\hat{\mathcal{I}}_{os}(t) = 1 - \hat{I}_{os}(t)$. We did not investigate the effect of changing the calcium diffusion coefficient, because the longitudinal cGMP and calcium spread are strongly coupled due to calcium exchange through exchanger and cGMP gated channels.

Consistent with Eq. 42, the simulations confirm that the variance of $\hat{I}_{os}(t)$ is almost independent of cGMP diffusion (Fig. S10e-g). In contrast, the variance of the local currents $\hat{I}(n,t)$ strongly depends on the diffusional coupling between the compartments (Fig. S10a-d). Without longitudinal diffusion the compartments are independent and the variance $\hat{I}(n,t)$ is around $N_{comp} = 810$ times larger compared to $\hat{I}_{os}(t)$ (Fig. S10a,e). In this case, the spectrum in Eq. 43 can be considered as the average spectrum obtained from $N_{comp} = 810$ independent currents $\hat{I}(n,t)$. Without longitudinal cGMP diffusion, spontaneous PDE noise induces huge current fluctuations in a compartment (Fig. S10a). We further notice that such fluctuations that decrease the number of spontaneously activated PDE and thereby increase the local cGMP concentration (denoted by positive fluctuations)
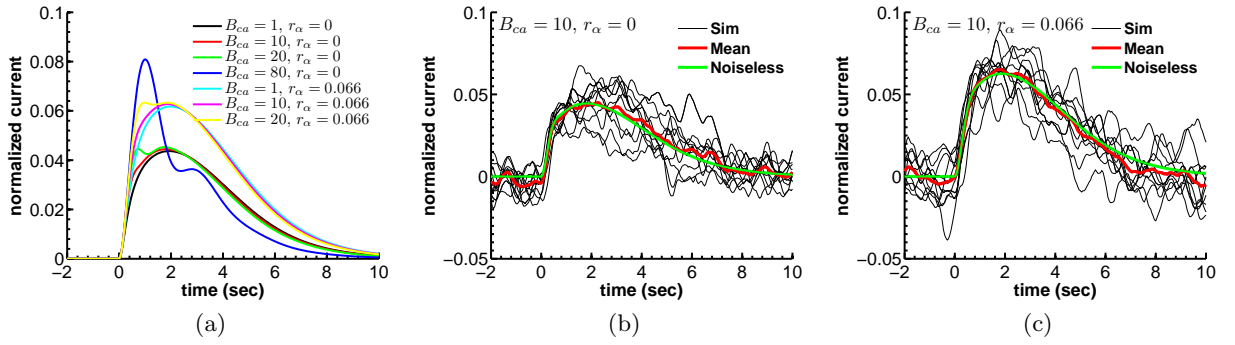
21

Fig. S9: **Single-photon response simulations for a toad rod with modified calcium feedback.** Parameters are as in Fig. 1 in the main text ($\beta_d = 1s^{-1}$ and $\gamma_{rt,max} = 200s^{-1}$), except for B_{ca} and r_α that have values as specified in the figure.(a) Superposition of noiseless simulations to show the effect of changing calcium feedback. The analytic curve shown in Fig. 1A in the main text is used for the number of light-activated PDE. (B) Superposition of 10 single-photon response simulations (black) with intrinsic noise for $B_{ca} = 10$ and $r_\alpha = 0$. There is no significant difference to the simulations with $B_{ca} = 0$ shown in Fig. 1 in the main text. (c) Superposition of 10 single-photon response simulations with $B_{ca} = 10$ and $r_\alpha = 0.066$. Time to peak is similar to (a), but the peak amplitude is increased by a factor 1.5 from 0.044 to 0.63. The standard deviation of the dark noise is increased by a a similar factor from around 0.08 to 0.12. The CV of the peak current in (a) and (b) is in both cases around 0.20. Except for the specified parameters, all parameters are as given in Table S3 and S4.
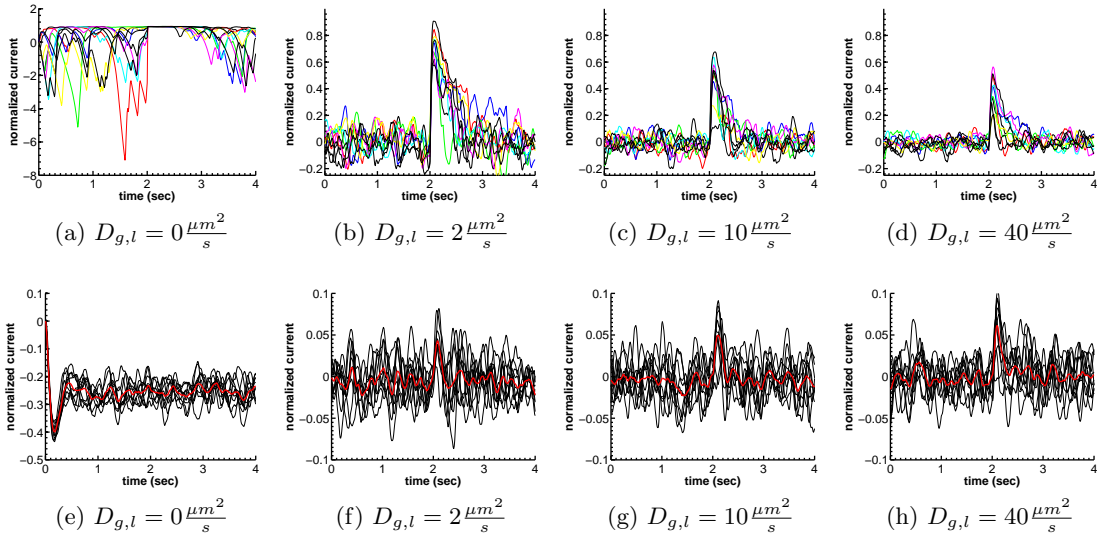
Fig. S10: **Effect of longitudinal cGMP diffusion on the dark noise and single-photon response in a mouse rod.** The longitudinal cGMP diffusion constant is as depicted in the figure. Each upper panel shows a superposition of 10 simulations of the normalized current $\hat{\mathcal{I}}(n,t)$ in the compartment where the photon is absorbed at time $t = 2s$. The lower panels show the corresponding normalized outer segment current $\hat{\mathcal{I}}_{os}(t)$ (red is the average).

have a much stronger impact on the current compared to such fluctuations that increase the number of spontaneously activated PDE and that decrease the local cGMP concentration (denoted by negative fluctuation). This asymmetry is due to the fact that only a small fraction of channels are open in darkness: a positive fluctuation additionally opens a large amount of channels leading to a large current influx, whereas a negative fluctuation can at most close all the channels and suppress the current. The large impact of such positive fluctuations also shifts the mean value of $\hat{\mathcal{I}}_{os}(t)$ from zero to -0.25 (Fig. S10a). Surprisingly, already a small longitudinal cGMP diffusion $D_{g,l} = 2\frac{\mu m^2}{s}$ strongly reduces the amplitude of the fluctuations (Fig. S10b,f). By further increasing longitudinal diffusion, the fluctuations of $\hat{I}(n,t)$ and $\hat{I}_{os}(t)$ become more and more similar (Fig. S10c,d,g,h). Indeed, for very fast longitudinal diffusion Eq. 43 can be considered as the power spectrum with only a single compartment where $\hat{I}(n,t)$ and $\hat{I}_{os}(t)$ have the same statistics.

Fig. S10 further illustrates how longitudinal diffusion affects the amplitude of a single-photon response locally and globally. Without diffusion, a single-photon absorption closes all the channels in the compartment where the photon is absorbed, $\hat{I}(n,t) = 0$ and $\hat{\mathcal{I}}(n,t) = 1 - \hat{I}(n,t) = 1$ (Fig. S10a). Although the local response is maximal in this case, the overall response is negligible (Fig. S10e). Longitudinal diffusion decreases the amplitude in the compartment where the photon is absorbed, but the spread of the signal increases the overall response. Surprisingly, the simulations reveal that the response amplitude and dark noise level change only little by increasing the diffusion from $D_{g,l} = 10\frac{\mu m^2}{s}$ to $D_{g,l} = 40\frac{\mu m^2}{s}$ (Fig. S10c,d,g,h)).

We conclude that the exact value of the longitudinal cGMP diffusion is not a key parameter for the fidelity of the rod photon response, as long as diffusion does not become too restricted.

Table S1: Parameters for PDE activation

Parameter	Definition
$\bar{P}^*_{sp,comp}$	Mean number of spontaneous actived PDE molecules per compartment
$\bar{P}^*_{li,max}$	Mean of the peak number of light-activated PDE
ρ_{pde}	PDE surface density
ν_{sp}	Spontaneous PDE activation rate
μ_{sp}	Spontaneous PDE deactivation rate
μ_{li}	Deactivation rate for light-activated PDE
τ_{rh}	Activated Rhodopsin lifetime
N_p	Number of Rhodopsin phosphorylation steps
$\gamma_{rt,max}$	Maximal transducin activation rate
ω	Decay rate of transducin activation with the number of phosphorylation steps
γ_{tp}	Rate by which activated transducin activates PDE

Table S2: Parameters for the photocurrent simulation

Parameter	Definition
N_{comp}	Number of compartments
R	OS radius
h	Compartment height
w	Disk width
a	Reaction radius for cGMP hydrolysis by an activated PDE molecule
k_{enc}	Encounter rate between a cGMP and an activated PDE molecule
k_{li}	Rate constant for cGMP hydrolysis by a light-activated PDE
k_{sp}	Rate constant for cGMP hydrolysis by a spontaneous activated PDE Determined from the equation $\beta_d = k_{sp}\bar{P}^*_{sp,comp}$
β_d	cGMP hydrolysis rate in the dark
g_d	cGMP concentration in the dark
c_d	Free calcium concentration in the dark
$I_{os,d}$	OS current in the dark
f_{ca}	Fraction of current carried by calcium
B_{ca}	Buffering capacity for calcium
K_α	Michaelis constant for cGMP synthesis
K_{ch}	Michaelis constant for channel opening
K_{ex}	Michaelis constant for calcium exchanger
n_α	Hill coefficient for cGMP synthesis
r_α	Ratio of minimal to maximal cGMP synthesis rate
n_{ch}	Hill coefficient for channel opening
D_g	Radial cGMP diffusion constant
D_{ca}	Radial calcium diffusion constant
$D_{g,l}$	Effective longitudinal cGMP diffusion constant
$D_{ca,l}$	Effective longitudinal calcium diffusion constant
γ_d	Rate for calcium exchange

Table S3: Parameters used to simulate PDE activation

Parameter	Toad	Mouse
$\bar{P}^*_{sp,comp}$	1.25	0.9
$\bar{P}^*_{li,max}$	150	8.2
$\mu_{sp}(\mathrm{s}^{-1})$	1.8	12.4
$\mu_{li}\ (\mathrm{s}^{-1})$	0.625	5
$\tau_{rh}\ (\mathrm{s})$	3	0.04
N_p	6	6
$\gamma_{rt,max}\ (\mathrm{s}^{-1})$	200	350
ω	0.1	0.1
$\gamma_{tp}\ (\mathrm{s}^{-1})$	300	300

Table S4: Parameter values used to simulate the photocurrent

Parameter	Toad	Mouse
N_{comp}	2000	810
R (μm)	3	0.7
h (nm)	15	15
w (nm)	15	15
a (nm)	3	3
$k_{enc}(\text{s}^{-1})$	2.9	61
$k_{li}(\text{s}^{-1})$	2.9	61
β_d (s^{-1})	1	4.1
g_d (μM)	3	3
c_d (μM)	0.3	0.3
$I_{os,d}$ (pA)	40	17.9
f_{ca}	0.12	0.12
γ_d (s^{-1})	92	23.4
B_{ca}	1	80
K_{α} (μM)	0.15	0.1
K_{ch} (μM)	20	20
K_{ex} (μM)	1.6	1.6
n_{α}	2	2
r_{α}	0	0.066
n_{ch}	3	3
D_g $(\mu m^2 s^{-1})$	150	150
D_{ca} $(\mu m^2 s^{-1})$	15	15
$D_{g,l}$ $(\mu m^2 s^{-1})$	20	40
$D_{ca,l}$ $(\mu m^2 s^{-1})$	2	2

References

[1] Reingruber J, Holcman D (2008) Estimating the rate of cgmp hydrolysis by phosphodiesterase in photoreceptors. *J Chem Phys* 129:145192.

[2] Nickell S, Park PSH, Baumeister W, Palczewski K (2007) Three-dimensionsal architecture of murine rod outer segemnts determined by cryoelectron tomography. *J of Cell Biol* 177:917–25.

[3] Y T (1987) The number, depth and elongation of disc incisures in the retinal rod of rana catesbeiana. *Exp Eye Res* 45:105–16.

[4] J R (1977) New aspects of the ultrastructure of frog rod outer segments. *Int Rev Cytol* 50:25–158.

[5] Cohen A (1960) The ultrastructure of the rods of the mouse retina. *Am J Anat* 107:2348.

[6] Holcman D, Korenbrot J (2004) Longitudinal diffusion in retinal rod and cone outer segment cytoplasm: The consequence of the cell structure. *Biophys J* 86:2566–2582.

[7] Caruso G, et al. (2006) Modeling the role of incisures in vertebrate phototransduciton. *Biophys J* 91:1192–1212.

[8] M N, Haeri M, Knox B, Schiesser W, Calvert P (2012) Photoreceptor signaling: supporting vision across a wide range of light intensities. *J Gen Physiol* 140:249–66.

[9] Calvert PD, et al. (2001) Membrane protein diffusion sets the speed of rod phototransduction. *Nature* 411:9094.

[10] Bisegna P, et al. (2008) Diffusion of the second messengers in the cytoplasm acts as a variability suppressor of the single photon response in vertebrate phototransduction. *Biophys J* 94:3363–3383.

[11] Yau KW, Hardie R (2009) Phototransduction motifs and variations. *Cell* 139:246 – 264.

[12] Burns M, Pugh J EN (2011) Lessons from photoreceptors: turning off g-protein signaling in living cells. *Physiology (Bethesda)* 25:72–84.

[13] Chen J, et al. (2010) Channel modulation and the mechanism of light adaptation in mouse rods. *J Neurosci* 30:16232–16240.

[14] Gillespie DT (1976) General method for numerically simulating stochastic time evolution of coupled chemical-reactions. *J Comp Phys* 22:403–434.

[15] Rieke F, Baylor D (1996) Molecular origin of continous dark noise in rod photoreceptors. *Biophys J* 71:2553–2572.

[16] Reingruber J, Holcman D (2008) The dynamics of phophodiesterase activation in rods and cones. *Biophys J* 94:1954–70.

[17] Hamer R, Nicholas S, Tranchina D, Liebman P, Lamb T (2003) Multiple steps of phosphorylation of activated rhodopsin can account for the reproducibility of vertebrate rod single-photon responses. *J Gen Physiol* 122:419–444.

[18] Hamer R, Nicholas S, Tranchina D, Lamb T, Jarvinen J (2005) Toward a unified model of vertebrate rod phototransduction. *Vis Neurosci* 22:417–436.

[19] Andreucci D, Bisegna P, Caruso G, Hamm H, DiBenedetto E (2003) Mathematical model of spatio-temporal dynmamics of second messengers in visual transduction. *Biophys J* 85:1358–76.

[20] Caruso G, et al. (2005) Mathematical and computational modelling of spatio-temporal signalling in rod phototransduction. *IEE Proc Syst Biol* 152:119–137.

[21] Shen L, et al. (2010) Dynamics of mouse rod phototransduction and its sensitivity to variation of key parameters. *IET Syst Biol* 4:12–32.

[22] Rieke F, Baylor D (1998) Origin of reproducibility in the responses of retinal rods to single photons. *Biophys J* 75:1836–1857.

[23] Whitlock G, Lamb T (1999) Variablity in the time ourse of single photon responses from toad rods: termination of rhodopsin's activity. *Neuron* 23:337–351.

[24] Field G, Rieke F (2002) Mechanisms regulating variability of the single-photon responses of mammalian rod photoreceptors. *Neuron* 35:733–747.

[25] Caruso G, et al. (2011) Identification of key factors that reduce the variability of the single photon response. *Proc Natl Acad Sci U S A* 108:7804–7.

[26] Burns M, Pugh Jr E (2009) Rgs9 concentration matters in rod phototransduction. *Biophys J* 16:1538–47.

[27] Chen C, Woodruff M, Chen F, Chen D, Fain G (2010) Background light produces a recoverin-dependent modulation of activated-rhodopsin lifetime in mouse rods. *J Neurosci* 30:1213–1220.

[28] Woodruff M, et al. (2008) Modulation of phosphodiesterase6 turnoff during background illumination in mouse rod photoreceptors. *J Neurosci* 28:2064–2074.

[29] Gross O, Pugh EN, Burns M (2012) Spatiotemporal cgmp dynamics in living mouse rods. *Biophys J* 102:1775–1784.

[30] Krispel C, et al. (2006) Rgs expression rate-limits recovery of rod photoresponses. *Neuron* 51:409–16.

[31] Rieke F, Baylor D (1998) Single-photon detection by rod cells of the retina. *Rev of Mod Phys* 70:1027–1036.

[32] Pugh Jr E, Lamb T (2000) Phototransduction in vertebrate rods and cones: Molecular mechanism of amplification, recovery and light adaptation. *In Handbook of Biological Physics Vol 3, Elsevier Science B V, Amsterdam* :183–255.

[33] Nikonov S, Engheta N, Pugh Jr E (1998) Kinetics of recovery of the dark-adapted salamander rod photoresponse. *J Gen Physiol* 111:7–37.

[34] Baylor D, Lamb T, Yau KW (1979) Responses of retinal rods to single-photons. *J Physiol* 288:613–634.

[35] Leskov I, et al. (2000) The gain of rod phototransdcuction:reconciliation of biochemical and electrophysiological measurements. *Neuron* 27:525–537.

[36] Nymark S, Heikkinen H, Haldin C, Donner K, Koskelainen A (2005) Light responses and light adaptation in rat retinal rods at different temperatures. *J Physiol* 567:923–38.

[37] Robinson D, Ratto G, Lagnado L, McNaughton P (1993) Temperature dependence of the light response in rat rods. *J Physiol* 462:465–81.

[38] Heck M, Hofmann K (2001) Maximal rate and nucleotide dependence of rhodopsin-catalyzed transducin activation: initial rate analysis based on a double displacement mechanism. *J Biol Chem* 276:10000–10009.

[39] Reingruber J, Holcman D (2009) Diffusion in narrow domains and application to phototransduction. *Phys Rev E* 79:030904.

[40] Pugh Jr E, Lamb T (1993) Amplification and kinetics of the activation steps in phototransduction. *Biochim et Biophys Acta* 1141:111–149.

[41] Nikonov S, Lamb T, Pugh Jr E (2000) The role of steady phosphodiesterase activity in the kinetics and sensitivity of the light-adapted salamander rod photoresponse. *J Gen Physiol* 116:795–824.

[42] Hodgkin A, Nunn BJ (1988) Control of light sensitive current in salamander rods. *J Physiol* 403:439–471.

[43] Cornwall M, Fain G (1994) Bleached pigment activates transduction in isolated rods of the salamander retina. *J Physiol* 480:261–279.

[44] Koutalos Y, Nakatani K, Yau KW (1995) Cyclic gmp diffusion coefficient in rod photoreceptors outer segment. *Biophys J* 68:373–382.

[45] Makino C, et al. (2012) Enzymatic relay mechanism stimulates cyclic gmp synthesis in rod photoresponse: biochemical and physiological study in guanylyl cyclase activating protein 1 knockout mice. *PLoS One* 7:e47637.

[46] Dizhoor A, Olshevskaya E, Peshenko I (2010) Mg2+/ca2+ cation binding cycle of guanylyl cyclase activating proteins (gcaps): role in regulation of photoreceptor guanylyl cyclase. *Mol Cell Biochem* 334:117–124.

[47] Mendez A, et al. (2001) Role of guanylate cyclase-activating proteins (gcaps) in setting the flash sensitivity of rod photoreceptors. *Proc Natl Acad Sci U S A* 98:9948–9953.

[48] Peshenko I, Dizhoor A (2006) Ca2+ and mg2+ binding properties of gcap-1. evidence that mg2+-bound form is the physiological activator of photoreceptor guanylyl cyclase. *J Biol Chem* 281:23830–41.

[49] Peshenko I, Dizhoor A (2004) Guanylyl cyclase-activating proteins (gcaps) are ca2+/mg2+ sensors: implications for photoreceptor guanylyl cyclase (retgc) regulation in mammalian photoreceptors. *J Biol Chem* 279:16903–6.

[50] Palczewski K, Polans A, Baehr W, Ames J (2000) Ca(2+)-binding proteins in the retina: structure, function, and the etiology of human visual diseases. *Bioessays* 22:337–50.

[51] Yau K, Baylor D (1989) Cyclic gmp-activated conductance of retinal photoreceptor cells. *Annu Rev Neurosci* 12:289–327.

[52] Cervetto L, Lagnado L, Perry R, Robinson D, McNaughton P (1989) Extrusion of calcium from rod outer segments is driven by both sodium and potassium gradients. *Nature* 337:740–743.

[53] Fain G (2011) Adaptation of mammalian photoreceptors to background light: putative role for direct modulation of phosphodiesterase. *Mol Neurobiol* 44:374–82.

[54] Gross O, Pugh EN, Burns M (2012) Calcium feedback to cgmp synthesis strongly attenuates single-photon responses driven by long rhodopsin lifetimes. *Neuron* 76:370–82.